Materials & Design 241 (2024) 112944

Contents lists available at ScienceDirect

Materials & Design

journal homepage: www.elsevier.com/locate/matdes

Effect of laser power and deposition sequence on microstructure of GRCop42 - Inconel 625 joints fabricated using laser directed energy deposition

Jakub Preis [a,b], Zexiao Wang [c], Jana Howard [d], Yu Lu [d], Nick Wannenmacher [b], Sheng Shen [c], Brian K. Paul [a,b], Somayeh Pasebani [a,b,*]

[a] School of Mechanical, Industrial, and Manufacturing Engineering, Oregon State University, Corvallis, OR, 97331, United States of America
[b] Advanced Technology and Manufacturing Institute (ATAMI), Oregon State University, Corvallis, OR, 97330, United States of America
[c] Department of Mechanical Engineering, Carnegie Mellon University, Pittsburgh, PA 15213, United States of America
[d] Boise State University, Center for Advanced Energy Studies, 997 MK Simpson Blvd, Idaho Falls, ID 83401, United States of America

ARTICLE INFO

Keywords:
Inconel 625
GRCop
Microstructure
Dissimilar metal joint
Laser directed energy deposition

ABSTRACT

The joining of Inconel 625 and GRCop42 using additive manufacturing is required for thermal management of high operating temperature components such as rocket combustion chambers. Though prior efforts have been made to use laser directed energy deposition to join these materials, the impact of laser power and deposition sequence on microstructure of these joints is not well understood. In this study, Inconel 625 onto GRCop42 and GRCop42 onto Inconel 625 joints are fabricated by powder directed-energy-deposition at various laser powers and subsequently subjected to characterization in terms of present defects, grain morphology, and phases. Results show lack-of-fusion free Inconel 625 onto GRCop42 joints can be fabricated by increasing the laser power in the first layer. Substrate remelting in GRCop42 onto Inconel 625 joints is found to result in a melt pool composition which induces liquid-state immiscibility, resulting in a Cu-deprived liquid solidifying to form crack prone islands. Increasing laser power decreases the embrittlement of these islands due to the precipitation of a lower volume fraction of intermetallic phases.

1. Introduction

Multi-metal additive manufacturing (AM) allows for the joining of dissimilar metals to fabricate components which have both spatially varying properties (i.e. thermal, physical, mechanical) and geometric complexity [1]. Such multi-property components are of particular interest for applications in the aeronautic and aerospace industry [2,3]. One application of particular interest for multi-metal AM is the combustion chamber within reusable liquid rocket engines. These chambers require regions of high thermal conductivity for heat dissipation along with regions of high-temperature strength [4]. Within such combustion chambers, Cu-based alloys are used as an interlayer, providing the necessary high thermal conductivity to efficiently transfer heat away from the chamber [5]. The Cu-based alloy is joined to a Ni-based superalloy, which is deposited as an external structural jacket providing high-temperature strength and oxidation resistance [6]. GRCop42 (Cu-based alloy developed at NASA Glenn Research Center) and Inconel 625 (Ni-based superalloy) are two alloys well suited for combustion chamber applications [7].

Currently, GRCop42 - Inconel 625 combustion chambers are fabricated by first fabricating the GRCop42 interlayer using laser powder bed fusion (LPBF) [5]. Afterwards, the Inconel external structural jacket is deposited onto the GRCop42 using wire electron beam directed energy deposition or powder laser directed energy deposition (LDED) [7,8]. Powder LDED has multi-material capability along with relatively high build rates, and could be used to fabricate the GRCop42 interlayer and Inconel 625 external structural jacket efficiently in a single build. Therefore, powder LDED of GRCop42, Inconel 625, and the GRCop42 - Inconel 625 joint must be thoroughly understood.

To serve an effective interlayer, powder LDED GRCop42 must have high thermal conductivity and high strength + ductility (i.e. minimal porosity). While no studies exist on the thermal conductivity of pow-

* Corresponding author at: School of Mechanical, Industrial, and Manufacturing Engineering, Oregon State University, Corvallis, OR, 97331, United States of America.
E-mail address: somayeh.pasebani@oregonstate.edu (S. Pasebani).

https://doi.org/10.1016/j.matdes.2024.112944
Received 17 January 2024; Received in revised form 16 March 2024; Accepted 14 April 2024
Available online 21 April 2024

der LDED GRCop42, the thermal conductivity of this alloy as fabricated by LPBF has been studied by Gradl et al. [5]. The authors reported that LPBF GRCop42 has the desired high thermal conductivity (275 W/mK at 25 °C). To ensure desired strength, LDED GRCop42 must be fabricated with minimal porosity. The porosity-free laser processing of Cu-based alloys such as GRCop42 is challenging due to high reflectivity and high thermal diffusivity [9]. To overcome this, Suresh et al. [10] used high laser powers of 1300-1375 W when fabricating GRCop42 thin walled structures using LDED. The printed structures had less than 0.1% porosity, indicating that the lack of fusion (LOF) typically associated with high reflectivity and high thermal diffusivity materials was avoided [11]. In addition, C15-Laves Cr_2Nb precipitates in the LDED printed GRCop42 were shown to be a similar size as in LPBF printed GRCop42 [10]. This is critical, since the Cr_2Nb precipitates reinforce the matrix resulting in high creep resistance necessary in prolonged lifecycle components such as combustion chambers [12]. Demeneghi et al. [13] studied the influence of wall thickness on tensile properties of GRCop42 printed using powder LDED. The authors found that a higher wall thickness is correlated with an increased elongation in unpolished specimens. When the specimens are polished, wall thickness is found to have no effect on the elongation, indicating that surface effects must be considered in LDED printed GRCop42 interlayers for combustion chambers. Based on the listed research, fabrication of GRCop42 by use of powder LDED results in the desired properties to serve as an effective interlayer.

To serve as an effective structural jacket, the powder LDED Inconel 625 must have desirable high temperature (HT) mechanical properties (thermal stability, high fatigue resistance, high yield strength, high creep strength). Hu et al. [14] investigated the thermal stability of powder LDED Inconel 625. The researchers reported a high recrystallization temperature (1200 °C), indicating that Inconel 625 via powder LDED can be expected to maintain high performance at high temperatures. Theriault et al. [15] studied the fatigue resistance of powder LDED Inconel 625. The researchers found that at both room temperature and 650 °C the powder LDED Inconel 625 has higher fatigue resistance than cast material and lower fatigue resistance than wrought material. Poudel et al. [16] studied the tensile deformation behavior of power LDED Inconel 625 at high temperatures, and found that dynamic recrystallization is found to occur above 650 °C resulting in lower yield strength. In addition, the researchers found that powder LDED Inconel 625 has a comparable yield strength to wrought Inconel 625 above 650 °C. While no studies have been conducted on creep strength of powder LDED Inconel 625, laser powder bed fusion Inconel 625 creep strength has been studied by Son et al. [17] who reported that LPBF Inconel 625 has a comparable creep strength to wrought Inconel 625 at 650 °C and 800 °C. Based on the listed research, powder LDED Inconel 625 can be expected to have the desirable mechanical properties required for structural reinforcement.

When joining Inconel 625 with GRCop42 using a liquid state process (such as powder - LDED), the two materials undergo Marangoni mixing at the interface creating a new mixing-induced alloy. This can lead to cracking at the interface due to various mechanisms (i.e. brittle phase formation, solidification cracking) [18]. Gradl et al. [4,6], Iams et al. [19], and Anderson et al. [20] reported no cracking in Inconel - GRCop joints fabricated using AM. In contrast, Gradl et al. [7] and Hales et al. [21] have reported cracking at the GRCop - Inconel interface, thus compromising the integrity of the joint life-cycle and ability to withstand loads. To understand the root cause of this cracking, the present authors [22] fabricated an array of GRCop42 - Inconel 625 mixture ratios by use of arc melting to mimic the remelting and dissimilar-metal mixing which takes place at the interface during liquid state joining. Results show that from 30 to 95 wt.% GRCop42, a lack of liquid state mixing (liquid-state immiscibility) occurs between a Cu-rich and Cu-deprived liquid, resulting in brittle phase formation from the Cu-deprived liquid at compositions corresponding to 60-95 wt.% GRCop42 [22]. This suggests that a process strategy is needed to help avoid these phases in an effort to fabricate defect-free GRCop42 - Inconel 625 joints. However, no published study has been conducted on the influence of processing parameters such as laser power on GRCop42 - Inconel 625 joint microstructure, presenting a critical literature gap.

A fundamental difficulty in fine-tuning parameters for multi-material AM is that the thermal conditions of a given laser pass are dependent on the thermal properties of the material surrounding the deposition zone. This means at a multi-material AM joint, the thermal history of a deposited material will depend on the thermal properties of a different material which was deposited in previous layers or laser passes. For example, Iams et al. [19] reported LDED of Inconel 718 onto GRCop42 results in far less remelting (i.e. smaller melt pool) than GRCop42 onto Inconel 718, due to GRCop42 rapidly diffusing thermal energy. Further complexity is added by the fact that during the joining of dissimilar metals by use of AM, remelting leads to inhomogeneous metal mixtures which have compositionally dependent thermal properties [23]. The effect of dissimilar thermal properties on GRCop42 - Inconel 625 joint properties are not available in literature.

In this work, an LDED system is used to fabricate GRCop42 - Inconel 625 joints using various laser powers to study the effect of energy density on defect formation and microstructure. To study the effect of deposition sequence on defect formation and microstructure, both Inconel 625 onto GRCop42 and GRCop42 onto Inconel 625 joints are fabricated. The joints are characterized in terms of defects (cracking and porosity), grain morphology, phases, and microhardness. The results of this work can be used as a processing strategy guide for the fabrication of crack free GRCop42 - Inconel 625 bimetallic joints.

2. Experimental methodology

2.1. Materials and LDED process

In this study, a Meltio M450 LDED machine was used for fabrication of GRCop42 - Inconel 625 joints. The M450 deposition head is equipped with six continuous wave lasers exhibiting a Gaussian distribution, each with a maximum power of 200 W (total maximum power 1200 W), and three powder delivery nozzles. Each laser is positioned at a 25° angle relative to the longitudinal axis (Z direction). A working distance of 7 mm was used, corresponding to the point where the lasers converge forming a single spot with a diameter of 0.9 mm. An image of the M450 system along with powder nozzles and laser exit ports is shown in Fig. 1.

Two deposition sequences were investigated: (1) Inconel 625 onto GRCop42 and (2) GRCop42 onto Inconel 625. The Inconel 625 substrate was fabricated by printing wire Inconel 625 using the M450 with a laser power of 500 W and a travel speed of 400 mm/min. The GRCop42 substrate was fabricated by printing power GRCop42 using the M450 with a laser power of 800 W, a travel speed of 400 mm/min, and a power feed rate of 2 g/min. Each substrate was milled flat to create a smooth surface for further deposition. The composition of the Inconel 625 and GRCop42 substrates is shown in Table 1. The substrate build plate was held at 16 °C. For joint fabrication, six 20 mm x 20 mm layers of Inconel 625 or GRCop42 powder were deposited onto the respective substrates, as shown in Fig. 2. Inconel 625 powder was purchased from Carpenter Additive, and the GRCop42 powder was purchased from Powder Alloy Corporation. The particle size distribution (PSD) of the powder was measured using a Malvern Particle size analyzer Mastersizer 3000. The composition and PSD of each feedstock can be referenced in Table 1. Optical micrographs of the powder are shown in Appendix A.

For all prints, a hatch spacing of 0.5 mm was used along with a powder feed rate of 2 g/min and a travel speed of 400 mm/min. For each layer, the hatching direction was rotated by 90° as shown in Fig. 2a. The effect of processing parameters on the joint was studied by varying the laser power from 200 - 800 W in increments of 200 W. To protect against oxidation, nitrogen was used as shielding and carrier gas with a flow rate of 10 L/min.

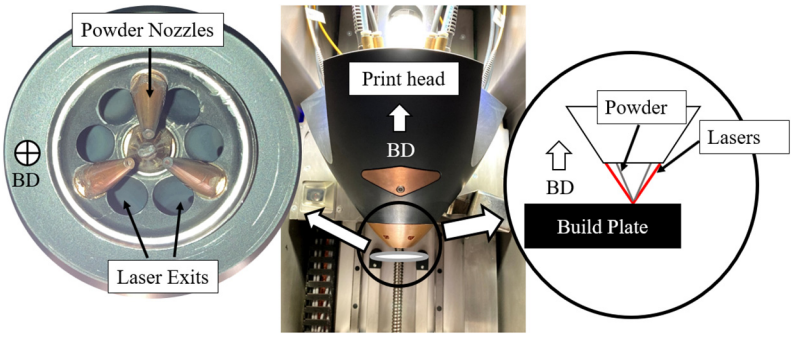

Fig. 1. Picture and schematic of Meltio M450 print head, powder nozzles, and laser exit locations.

Table 1
Composition and PSD pertaining to GRCop42 and Inconel 625 powder along with substrate composition.

Material	D10 µm	D50 µm	D90 µm	Ni *wt.%*	Cr *wt.%*	Nb *wt.%*	Ta *wt.%*	Mo *wt.%*	Cu *wt.%*	Fe *wt.%*	Al *wt.%*	Other *wt.%*
Inconel 625 Substrate	-	-	-	64.8	22.2	3.49		8.6	0.002	0.2	0.12	0.588
GRCop42 Substrate	-	-	-	-	3.3	2.7	-	-	*Bal*	-	-	-
Inconel 625 Powder	40.5	72.7	124	63.2	21.5	3.97		9.2	-	0.85	0.24	1.04
GRCop42 Powder	44.4	65.4	95.7	-	3.3	2.7	-	-	*Bal*	-	-	-

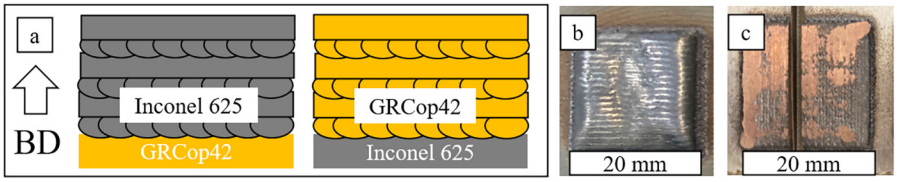

Fig. 2. (a) Schematic of deposition sequences investigated. (b) Inconel 625 deposited onto a GRCop42 substrate, and (c) GRCop42 deposited onto an Inconel 625 substrate with an EDM cutout for microstructure characterization.

2.2. Microstructure characterization

To investigate the microstructure of the joints, samples were cut using wire electronic discharge machining to expose the surface along the build direction. The samples were mounted and ground using SiC papers from 180 to 1200 grit. The samples were then polished using a 1 µm alumina slurry, followed by a 0.05 µm alumina slurry, and then a 0.05 µm silica solution. Lastly, the samples were vibratory polished for 12 hours using a 0.02 µm silica solution. To reveal the microstructure, the samples were chemically etched for 2 seconds using Ferric Chloride ($FeCl_3$) which targets Cu-rich compositions. A Zeiss Axiotron optical microscope was used to investigate joint microstructure and morphology.

To identify present phases, a FEI Quanta 3D dual-beam focused ion beam (FIB)/ scanning electron microscope (SEM) was used to extract a lamellae from a region of interest and mill it to a thickness of <120 nm. Both sides of the lamella were milled with 2 kV Ga^+ as a final step to minimize the FIB induced damage. The lamellas surfaces were cleaned using a Fischione Model 1040 Nanomill with a low beam energy of 700 eV Ar^+, to further remove the Ga^+ damaged layers from the FIB process. A Thermo Fisher Spectra 300 scanning transmission electron microscope (S-TEM) with an accelerating voltage of 300 keV was used to extract selected area diffraction (SAD) patterns for crystal structure identification. All TEM sample preparation and analysis was carried out at the Microscopy and Characterization Suite at the Center for Advanced Energy Studies (CAES).

To characterize phase morphology, a Helios 650 Ultra Resolution Dual Beam SEM was used to collect electron backscatter images of the sample. A FEI Quanta 3D dual beam scanning electron microscope (SEM) equipped with energy dispersive X-ray spectroscopy (EDS) and electron backscatter diffraction (EBSD) detectors was used to measure elemental composition and characterize the grain morphology. An accelerating voltage of 20 eV and a beam current of 1.8 nA was used. The EBSD images were collected using a step size of 1.4 µm and cleaned using grain dilation in AMETEK OIM software with a minimum grain size of 1 and a grain tolerance angle of 5 (these are dimensionless parameters in the software).

To scan for defects in three dimensions, computer tomographic (CT) imaging was performed using a Zeiss Xradia Context MicroCT. A voltage of 160 kV and a voxel size of 2.6 µm was used. Visualization and analysis was conducted using the Dragonfly software.

Vickers microhardness was used to gauge local mechanical properties within the joint. A Leco LM-248AT machine was used with a load of 500 gf and a 15 s dwell time. A minimum of 10 indents were collected to obtain the average and standard deviation for each region of interest.

2.3. Thermal conductivity profile

The thermal conductivity of the GRCop42 - Inconel 625 joint structure was characterized by a frequency domain thermoreflectance (FDTR) system. The FDTR system achieves fast and non-contact thermal characterizations through a pair of lasers aligned at the measurement point [24]. A pump laser with wavelength of 405 nm inputs a periodically modulated heat flux on the sample surface, while a probe laser with wavelength of 532 nm detects the surface temperature change induced by the pump laser. The two lasers have calibrated radii of 16.50 µm. For each location of interest, the phase difference between the modulated pump laser and reflected probe laser was recorded under different modulation frequencies, and the thermal conductivity of the sample was determined through a curve-fitting process to an analytical heat conduction model [25]. To maximize the signal to noise ratio during the pump-probe measurement, a 120-nm thick gold film was deposited as the transducer on the polished samples by sputter-

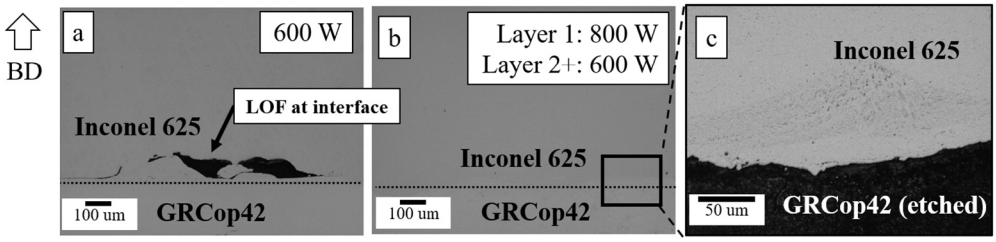

Fig. 3. Optical micrographs of Inconel 625 deposited onto a GRCop42 substrate at (a) 600 W unetched, (b) 800 W in the first layer of Inconel 625 followed by 600 W for subsequent layers unetched, and (c) etched high magnification image of the joint shown in (b). For the etched micrograph, dark regions are Cu-rich while gray regions are Cu-deprived.

Table 2
Summary of Inconel 625 onto GRCop42 and GRCop42 onto Inconel 625 joint defects for each laser power tested.

Laser Power *W*	Inconel onto GRCop42	GRCop42 onto Inconel
200	No adhesion	LOF in layers 2+
400	No adhesion	Cracking in islands
600	LOF at interface	Cracking in islands
800*	No defects	No cracking, islands present

* For the 800 W Inconel 625 onto GRCop42 sample, the laser power was decreased to 600 W in layers 2+ to prevent vaporization of the material.

ing. For each GRCop - Inconel joint sample, the thermal conductivity was scanned across the material interface with the increment of 0.5 mm, revealing the transition from the low thermal conductivity Inconel 625 region towards the GRCop-42 region with relatively higher thermal conductivity.

2.4. Computation

The CALculation of PHAse Diagrams (CALPHAD) approach was used to conduct a computational study of equilibrium and non-equilibrium (Scheil without back-diffusion) phases in order to assist in analysis of the solidification path at each composition of interest. To extract phases as a function of temperature and composition, Thermo-Calc (version 2023a) TC-python API was used in conjunction with a Python code. Both TCCU5 (Cu-based alloys optimized database) [26] and TCNI12 (Ni-based alloys optimized database) [27] were used. To limit computational cost, only Cu, Ni, Cr, Mo, and Nb were considered.

3. Results

3.1. Joint defects

Table 2 provides an overview of the Inconel 625 onto GRCop42 joint defects for the tested laser powers. For the Inconel 625 onto GRCop42 joint, no adhesion was observed between the Inconel 625 and GRCop42 substrate at laser powers of 200 W and 400 W. At 600 W, lack-of-fusion (LOF) was observed within the first layer of the deposited Inconel 625 as shown in Fig. 3a. This is attributed to the high thermal diffusivity of the GRCop42 substrate (80 mm^2/s for GRCop42, 2.9 mm^2/s for Inconel 625), discussed in Section 4.1. When Inconel 625 was deposited using 800 W, the added energy resulted in no LOF as shown in Fig. 3b. After the first 800 W layer, the laser power was decreased to 600 W to avoid vaporization of the material which occurs when the melt pool reaches an excessively high temperature. The etched high magnification image of the 800 W joint in Fig. 3c shows bonding along with a lack of mixing-induced brittle phases, indicating a defect-free joint was achieved.

Fig. 4a-d shows etched optical micrographs of GRCop42 deposited onto Inconel 625 using 200, 400, 600 and 800 W respectively. Two Cu-deprived (gray in Fig. 4a-d) microstructural features are of interest; peninsulas and islands. The mechanism of island and peninsula formation will be further discussed in section 4.2. Peninsulas extend from the Inconel 625 into the deposited GRCop42 along the interface. Islands are

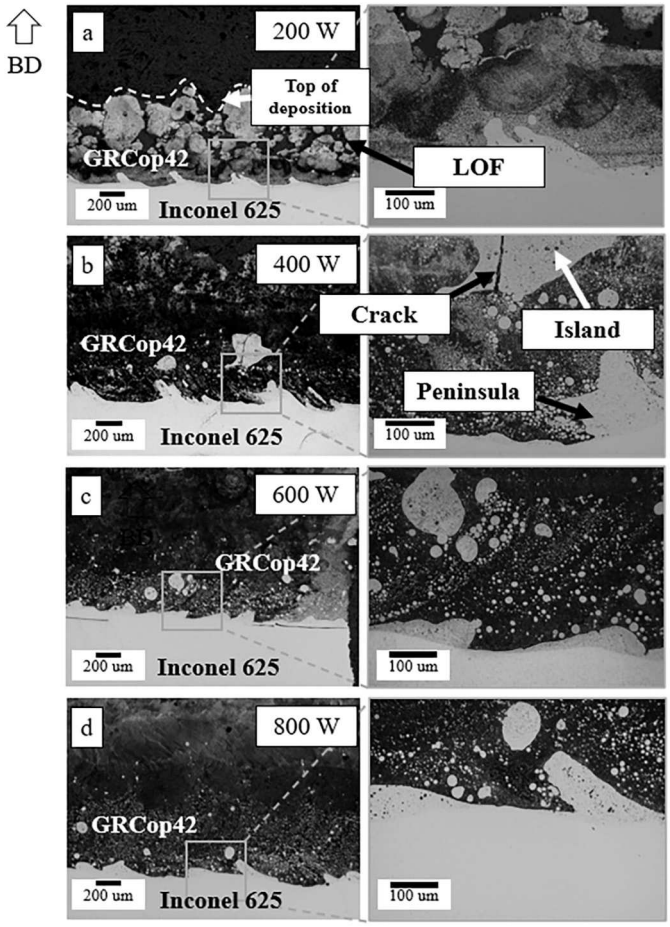

Fig. 4. Etched optical micrographs of GRCop42 deposited onto a Inconel 625 substrate at (a) 200 W, (b) 400 W, (c) 600 W, and (d) 800 W. Dark regions are Cu-rich while gray regions are Cu-deprived.

Cu-deprived structures observed above the interface fully surrounded by GRCop42. The 200 W joint (Fig. 4a) shows small peninsulas and a near complete lack of islands, along with LOF in the GRCop42 due to the low energy density used. In the 400 W and 600 W joint, cracking was observed within the islands as shown in Fig. 4b. To confirm no cracking is present within the 800 W joint, the sample was CT scanned for defects in three dimensions. The results, shown in Appendix B, indicate no cracking in the 800 W joint islands.

3.2. Compositional profile

EDS line scans were collected at the interface for both deposition sequences. For the Inconel 625 onto GRCop42 joint, the 800 W parameter is the only LOF free joint and was therefore selected for EDS analysis. For the GRCop42 onto Inconel 625 joint, both the 400 W and 800 W

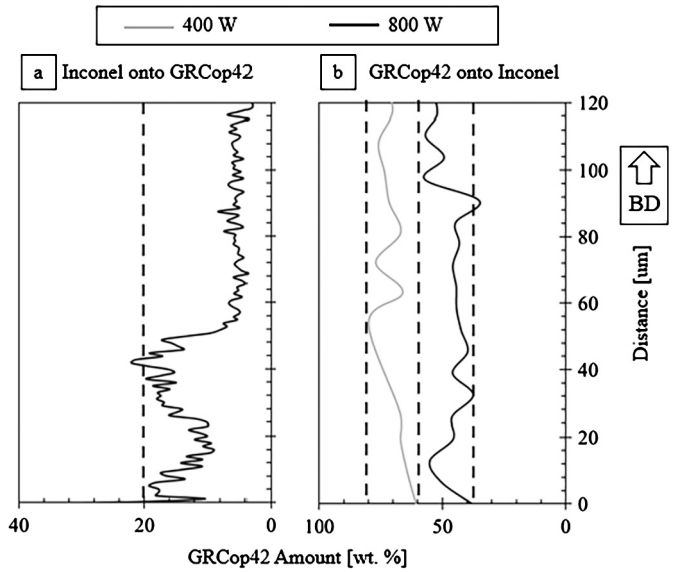

Fig. 5. EDS line scan directly above the interface of (a) Inconel 625 deposited onto GRCop42 and (b) GRCop42 deposited onto Inconel 625. The dashed lines show the compositional range measured for each laser power. The GRCop42 wt. % shown in the graph was calculated based on the measured Cu wt. %.

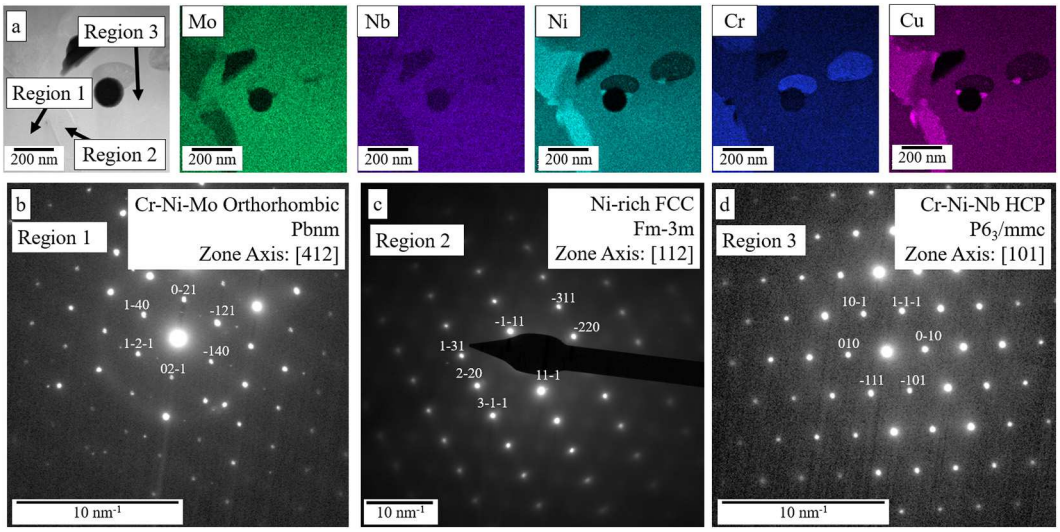

Fig. 6. (a) STEM-EDS maps with corresponding SAD patters of the (b) the Cr-Ni-Mo P-phase along the [412] zone axis, (c) the Ni-Cu phase along the [112] zone axis, and (d) Cr-Ni-Nb C14-Laves phase along the [101] zone axis. The numbers in (a) indicate region of SAD pattern collection.

joints were subject to EDS line scans to understand the impact of laser power on the distribution of the composition directly above the interface. The results are shown in Fig. 5a, b, with dashed lines specifying the measured compositional range. As shown in Fig. 5a, for the 800 W Inconel 625 onto GRCop42 joint, the composition reaches a maximum value of 20 wt.% GRCop42. For the GRCop42 onto Inconel 625 joint, a greater GRCop42 amount is measured above the interface for the 400 W joint (between 60 and 80 wt.% GRCop42) as compared with the 800 W joint (between 40 and 60 wt.% GRCop42). This result can be explained the higher laser power in the 800 W joint resulting in an increased amount of the Inconel 625 substrate remelting, leading to the proportionally lower GRCop42 amount measured above the interface. EDS line scans showing the elemental distributions on a larger length scale are provided in Appendix C.

3.3. Phase analysis and microhardness

The Inconel 625 onto GRCop42 joint showed only FCC phases, and was therefore not subject to further phase analysis. To further investigate cracking in the islands and characterize present phases in the GRCop42 onto Inconel 625 joint, a TEM sample was extracted from the middle of an island within the 400 W sample (i.e. the sample consisted completely of material from the island). The STEM image along with corresponding TEM-EDS images in Fig. 6a indicates the presence of three phases within the islands; a Cr-Ni-Mo rich phase (region 1), Ni-rich phase (region 2), and Cr-Ni-Nb rich phase (region 3). The TEM-EDS measured elemental compositions of each phase are provided in Table 3. The SAD pattern of the Cr-Ni-Mo rich phase (region 1) is presented in Fig. 6b and shows a primitive orthorhombic Pbnm-type crystal structure with a stoichiometric composition of $Cr_{18}Ni_{40}Mo_{42}$ [28]. This phase is commonly referred to as the P-phase in the Cr-Ni-Mo ternary phase diagram and is an equilibrium high temperature phase [28]. The Ni-Cu phase (region 2) constitutes a face centered cubic (FCC) solid solution as shown in Fig. 6c. The Cr-Ni-Nb phase in (region 3) has a hexagonal closed packed (HCP) $P6_3/mmc$ crystal structure [29], previously identified in GRCop42 - Inconel joints by both Preis et al. [22] and Iams et al. [19]. This phase is commonly referred to a C14-Laves or high temp Cr_2Nb [19]. Both the Cr-Ni-Mo P-phase and Cr-Ni-Nb C14-Laves phase are intermetallic and can contribute to the embrittlement of a material [18].

Table 3
STEM-EDS measured elemental compositions of regions from an island in the 400 W GRCop42 onto Inconel 625 sample.

Region	Phase	Cu *wt.%*	Ni *wt.%*	Cr *wt.%*	Mo *wt.%*	Nb *wt.%*
1	Cr-Ni-Mo P-Phase	11.1 ± 1.57	28.1 ± 3.29	33.0 ± 3.36	19.6 ± 2.27	8.1 ± 1.05
2	Ni-rich FCC	23.1 ± 3.02	43.1 ± 4.09	20.7 ± 2.66	5.0 ± 0.71	7.9 ± 1.08
3	Cr-Ni-Nb C14-Laves	11.5 ± 1.55	29.7 ± 3.26	20.7 ± 2.39	15.7 ± 1.81	22.3 ± 2.38

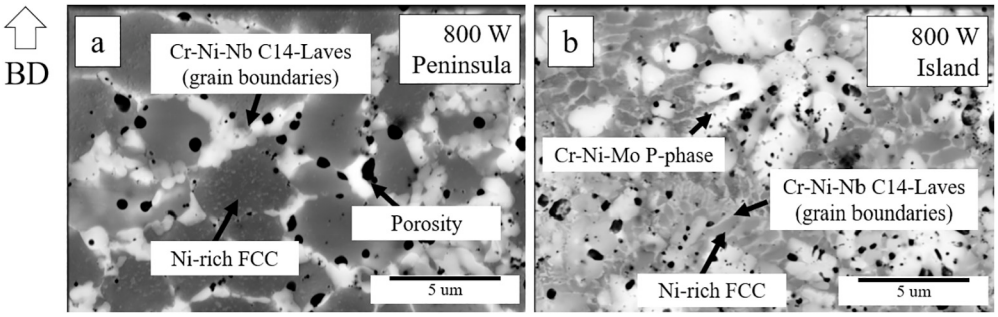

Fig. 7. Backscatter images of (a) the peninsula and (b) and island of the 800 W GRCop42 onto Inconel 625 sample.

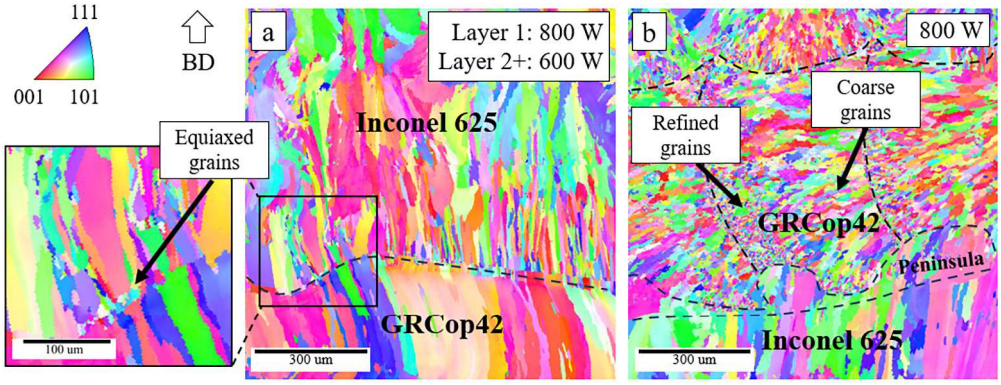

Fig. 8. EBSD crystal orientation maps of (a) Inconel 625 onto GRCop42 and (b) GRCop42 onto Inconel 625. Dashed lines specify bead cross section outlines along with location of the interface.

Table 4
Microhardness of islands and peninsulas in LDED GRCop42 deposited onto Inconel 625 as a function of laser power with Inconel 625 and GRCop42 microhardness values provided for reference.

Sample	Peninsula *HV.5*	Island *HV.5*
GRCop42 onto Inconel 400 W	382 ± 75	718 ± 159
GRCop42 onto Inconel 600 W	400 ± 105	665 ± 216
GRCop42 onto Inconel 800 W	401 ± 134	590 ± 215
Pure GRCop42	114 ± 28	
Pure Inconel 625	262 ± 27	

To gauge brittle phase impact on mechanical properties, the microhardness of islands and peninsulas in the 400, 600, and 800 W samples was measured as shown in Table 4. Both peninsulas and islands show a microhardness significantly higher than Inconel 625 (microhardness of pure LDED Inconel 625 was measured to be 271 ± 35 HV.5), suggesting embrittlement due to the presence of the intermetallic Cr-Ni-Nb C14-Laves phase and Cr-Ni-Mo P-phase. While the microhardness value of peninsulas is relatively constant for each laser power used, the island microhardness shows a decreasing trend with increased laser power. This effect is further discussed in section 4.2.

The 800 W sample is considered the best GRCop42 onto Inconel 625 joint and was subject to further characterization given that: (1) optical micrographs (Fig. 4d) show a lack of cracking and (2) microhardness values (Table 4) indicate a minimum value of embrittlement in the islands. To investigate phase morphology within the peninsula and islands above the interface, backscatter imaging was used as shown in Fig. 7a-b. In the peninsulas (Fig. 7a), the Cr-Ni-Nb C14-Laves phase is pushed toward the Ni-rich phase grain boundaries. The islands (Fig. 7b), by contrast, show irregular globular Cr-Ni-Mo P-phase regions, along with the Cr-Ni-Nb C14-Laves phase occupying the refined Ni-rich FCC grain boundaries.

3.4. Grain morphology

To further investigate the microstructure of the crack and LOF-free joints, an EBSD scan was performed on the 800 W Inconel 625 onto GRCop42 and GRCop42 onto Inconel 625 joints as shown in Fig. 8. The results show a lack of epitaxial growth in both joints. In the Inconel 625 onto GRCop42 joint (Fig. 8a), the GRCop42 substrate below the interface shows large grains elongated in the build direction, suggesting grain growth occurred due to the high energy density input when depositing the Inconel 625. The deposited Inconel 625 has refined equiaxed grains directly above the interface. Further above the interface, columnar grains elongated in the build direction are observed.

In the GRCop42 onto Inconel 625 joint (Fig. 8b), the GRCop42 shows a refined microstructure towards the left side of each bead, with columnar grains elongated along the axis parallel to the interface. This is explained by the fact that the beads are deposited left to right. When a

Table 5
Thermal and physical properties of GRCop42 and Inconel 625. The thermal diffusivity is calculated from the thermal conductivity, specific heat, and density.

Alloy	Thermal Conductivity *W/mK*	Specific heat *J/gK*	Density *g/cm^3*	Thermal diffusivity *mm^2/s*
GRCop42	275 [4]	0.384 [34]	8.85 [12]	80
Inconel 625	10 [35]	0.41 [35]	8.40 [35]	2.9

given GRCop42 bead is deposited, nucleation begins off of its previously deposited GRCop42 neighbor rather than the Inconel 625 lying below it due to the high thermal diffusivity of GRCop42 (thermal diffusivity of GRCop42 is 80 mm^2/s as shown in Table 5) resulting in a high cooling rate. This cooling rate combined with grain refinement through presence of Cr_2Nb precipitates results in refined grains observed towards the left side of the melt pool. Larger grains are observed to the right of each GRCop42 deposited bead due to grain growth which occurs from heat in subsequent bead deposition.

3.5. Thermal conductivity profile

The thermal conductivity line scan of the GRCop42 onto Inconel 625 joint was measured to understand the impact of Inconel 625 mixing on the thermal performance of the deposited GRCop42. The results, shown in Fig. 9, indicate a higher thermal conductivity for the 400 W joint as compared with the 800 W joint for all distances above the interface. This phenomenon can be explained by considering the EDS line scan in Fig. 5, which shows a lower GRCop42 wt.% in the 800 W joint than the 400 W joint due to increased Inconel 625 substrate remelting. Neither the 400 W nor the 800 W joint achieve the literature reported value of 275 W/mK [5] for thermal conductivity. The thermal conductivity of Cu has been shown to be very sensitive to Ni content; data by Ackerman et al. [30] reports a concentration as low as 3 wt.% Ni decreases the thermal conductivity of Cu by 50%. This highlights the importance of minimizing substrate remelting to allow for thermal efficiency of the GRCop42 in GRCop42 Inconel 625 joints.

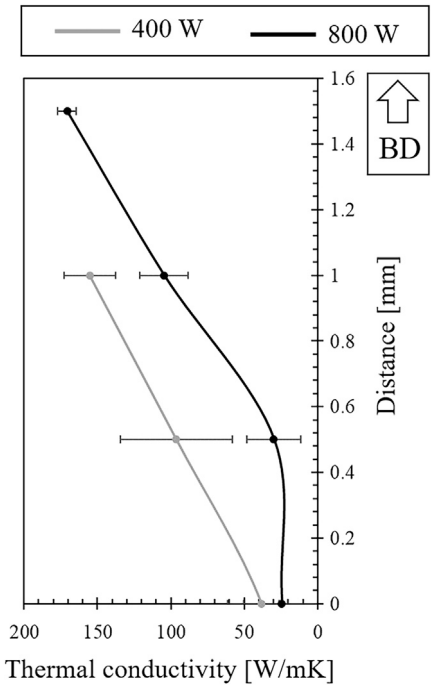

Fig. 9. Thermal conductivity profile above the interface for GRCop42 deposited onto Inconel 625. The thermal conductivity was not measured at 1.5 mm for the 400 W joint because the height of the deposited GRCop42 in this joint is less than 1.5 mm.

4. Discussion

4.1. Implication of deposition sequence on thermal history and microstructure of dissimilar GRCop42 - Inconel 625 joints

When depositing material using powder LDED, the substrate material properties constitute the lower boundary condition of the joint through which the heat from the laser is diffused. The adhesion of the material onto the substrate depends on the melt pool dimensions and peak temperature [31]. Previous works [32,33] have shown that depositing on a higher thermal diffusivity substrate decreases melt pool dimensions and peak melt pool temperature. As shown in Table 5 the thermal diffusivity of GRCop42 is 27 times higher than that of Inconel 625. This explains why no adhesion was observed when depositing Inconel 625 onto GRCop42 using 200 W and 400 W, while at the same laser powers the first layer of GRCop42 was successfully deposited onto Inconel 625 as shown in Table 2. In addition, the LOF observed in the 600 W Inconel onto GRCop42 joint can be explained by this concept; the high thermal diffusivity of GRCop42 results in a smaller melt pool and lower peak temperature, leading to insufficient melting of the Inconel 625 powder to create a continuous metallic bond at the interface.

In addition to affecting deposited material adhesion and LOF defects, the substrate material properties also govern the solidification characteristics (thermal gradient and solidification rate) at the joint, which in turn effect the grain morphology. As shown in Fig. 8a, when depositing Inconel 625 onto GRCop42 a lack of epitaxial growth is observed, with equiaxed grains observed directly above the interface. The presence of equiaxed grains can be attributed to a fast cooling rate when depositing onto the GRCop42 substrate. A lack of epitaxial growth in dissimilar metal joining has been shown to occur when there is a mismatch in crystal structure [36] (i.e. joining ferritic and austenitic steels), or when equiaxed grains are nucleated at the interface [37–39]. Since Inconel 625 and GRCop42 have a matching (FCC) crystal structure and have been shown to have a similar lattice constant (.360 nm for Inconel 625 [40] and .362 nm for GRCop42 [12]), it is likely the high thermal diffusivity of the GRCop42 substrate results in solidification conditions such that equiaxed grains are precipitated, preventing further epitaxial growth.

The lack of epitaxial growth in the GRCop42 onto Inconel 625 joint can be explained by the fact that the deposited GRCop42 has a higher thermal diffusivity than the Inconel 625 below it. As a subsequent GRCop42 bead is deposited, it solidifies off of the previously deposited bead (i.e. solidification occurs off of the left boundary), resulting in columnar grains elongated from left to right as shown in Fig. 8b. This prevents epitaxial growth, since the GRCop42 grains do not grow upward from the Inconel 625 interface.

4.2. Mechanism of island formation

When depositing GRCop42 onto Inconel 625, remelting of the Inconel 625 substrate along with Marangoni motion results in a liquid GRCop42 - Inconel 625 mixture within the melt pool. Within such mixtures, Preis et al. [22] show liquid state separation (liquid-state immiscibility) occurs between a Cu-deprived (<17 wt.% Cu) and a Cu-rich

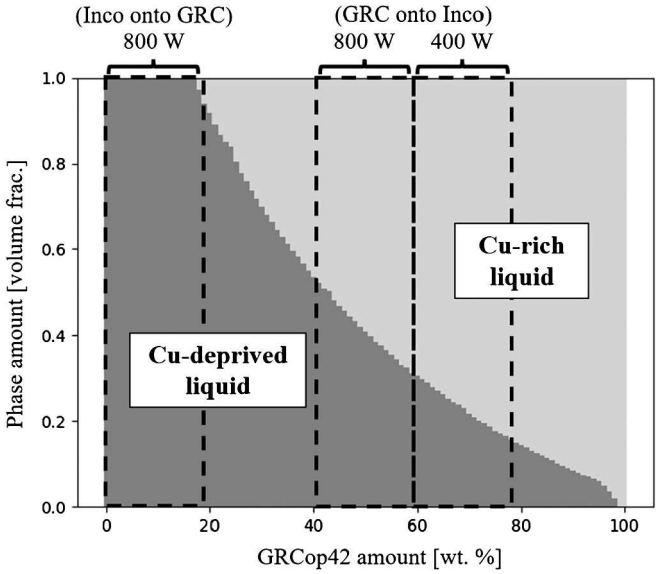

Fig. 10. CALPHAD software prediction of the volume fraction of the Cu-deprived and Cu-rich liquid phases as a function of GRCop42 wt.% at each composition's liquidus temperature. The dashed lines indicate the composition range from Fig. 5 above the interface for the Inconel 625 onto GRCop42 and GRCop42 onto Inconel 625 joints.

(>70 wt.% Cu) liquid phase. Fig. 10 shows the volume fraction of the Cu-deprived and Cu-rich liquid phases as predicted by CALPHAD at each compositions liquidus. For example, at 50 wt.% GRCop42, Fig. 10 shows that the volume fraction of the Cu-deprived liquid phase is .4 and the volume fraction of the Cu-rich liquid phase is .6. From Fig. 10, it can be seen that the liquid-state immiscibility is predicted to start at compositions corresponding to 20 wt.% GRCop42 and end at compositions corresponding to 98 wt.% GRCop42. Cu-deprived islands of the type shown in the GRCop42 onto Inconel 625 joint (Fig. 4b-d) have been previously observed in GRCop42 onto Inconel 718 joints via LDED [19], and are for the first time within the present study attributed to the presence of the liquid-state immiscibility. Within the melt pool, the Cu-deprived liquid separates and forms spherical structures (i.e. islands) to minimize surface energy. The lack of islands in the Inconel 625 onto GRCop42 joints (Fig. 3) is attributed to the fact that not enough GRCop42 substrate is remelted to elicit a miscibility gap. This is confirmed by the EDS line scan in Fig. 5a, which shows the GRCop42 wt.% is under 20 wt.% GRCop42 above the interface, and therefore under the threshold required to avoid the miscibility gap in the 800 W Inconel onto GRCop42 joint.

Upon separation, both the Cu-rich and Cu-deprived liquids follow independent solidification paths. The Cu-rich liquid forms a FCC Cu-rich phase [22]. The Cu-deprived liquid has been shown to form a number of intermetallic phases (i.e. C14-Laves, Nb_5Ni) [22]. To further understand at what compositions brittle intermetallic phases are predicted to form, CALPHAD was used to model equilibrium at solidus and Scheil (non-equilibrium) predicted phases as shown in Fig. 11. The equilibrium predictions assume an infinitely slow cooling rate, while the Scheil predictions assume an infinitely fast cooling rate [18]. Therefore, these two predictions represent extremes and the actual LDED cooling rate lies in between the equilibrium and Scheil assumptions. It should be noted that the TEM SAD pattern in Fig. 6b indicates the presence of the Cr-Ni-Mo P-phase, which is not predicted by the CALPHAD modeling in Fig. 11. In addition, CALPHAD modeling in Fig. 11a-b predicts three intermetallic phases (Mo-Nb-Cr BCC, $NbNi_5$, and Mo-Cr-Nb Rhombohedral) that were not detected within the LDED samples in this study. These inconsistencies could be due to the CALPHAD assumptions (i.e. slow cooling rate for equilibrium and infinitely fast cooling rate for scheil) or due to inaccuracies within the thermodynamic database used.

The lower hardness values in the 800 W GRCop42 onto Inconel 625 islands as compared to the 400 W and 600 W islands can be explained by the Cu-deprived liquid CALPHAD results in Fig. 11. As shown in Fig. 5, when using 400 W the composition above the interface of the GRCop42 onto Inconel 625 joint is between 60 and 80 wt.% GRCop42. When using 800 W, greater Inconel 625 substrate remelting results in a composition which is between 40 and 60 wt.% GRCop42. By mapping these compositions onto the CALPHAD predictions in Fig. 11a-b, it can be seen that the volume fraction of brittle phases (i.e. non Ni-rich FCC phases) is significantly lower at the compositional range induced at 800 W (i.e. greater Inconel 625 content, less GRCop42) as compared to the compositional range induced at 400 W. It should be noted that advanced coupled thermo-fluid modeling of dissimilar metal joining has shown the melt pool composition above interface can be inhomogeneous due to insufficient melt pool mixing [23]. This explains the large standard deviation observed in the island microhardness (Table 4). Depending on the localized composition within the melt pool, the Cu-deprived liquid can solidify to form islands with varying levels of brittle intermetallic phases.

Cracking in the 400 W and 600 W islands in the GRCop42 onto Inconel 625 joints occurs due to the high thermal strain induced during the LDED process [41]. The high volume fraction of the brittle (non Ni-FCC) phases in the islands impedes dislocation motion, resulting in the inability to resolve the thermal strain [18]. In contrast, the 800 W islands contain sufficient Ni-FCC volume fraction in the islands to resolve the thermal strain and prevent cracking.

5. Conclusion

In this study, the effect of laser power and deposition sequence on the defects and microstructure of GRCop42 - Inconel 625 joints was investigated. A summary of the findings is provided as follows:

- When depositing Inconel 625 onto GRCop42, lack of fusion occurs due to the high thermal diffusivity of the GRCop42 substrate. This is mitigated by increasing the laser power in the first layer of Inconel 625 deposition. If < 20 wt.% of the GRCop42 substrate is remelted, liquid-state immiscibility is avoided and a crack free bimetal joint can be fabricated.
- When depositing GRCop42 onto Inconel 625, remelting of the Inconel 625 substrate results in melt pool compositions which induce a lack of liquid state mixing between a Cu-rich and Cu-deprived liquid. The Cu-deprived liquid solidifies to form islands with Cr-Ni-Nb C14-Laves (HCP) and Cr-Ni-Mo P-phase (orthorhombic) intermetallic phases which are prone to cracking.
- Island embrittlement in GRCop42 onto Inconel 625 joints can be decreased by increasing laser power, leading to a greater amount of Inconel 625 substrate remelting in the first layer. This results in a greater volume fraction of Ni-rich FCC phase and lesser volume fraction of brittle intermetallic phases in the islands, thereby decreasing susceptibility of cracking.

While a Inconel onto GRCop42 joint was fabricated with no LOF and brittle phases, islands with brittle phases could not be completely eliminated from the GRCop42 onto Inconel 625 joint due to existence of liquid-state immiscibility in GRCop42 - Inconel 625 liquid mixtures. Therefore, future efforts should focus on developing transition compositions to be used between Inconel 625 and GRCop42 to avoid a liquid state separation (miscibility gap) and subsequent brittle phase formation.

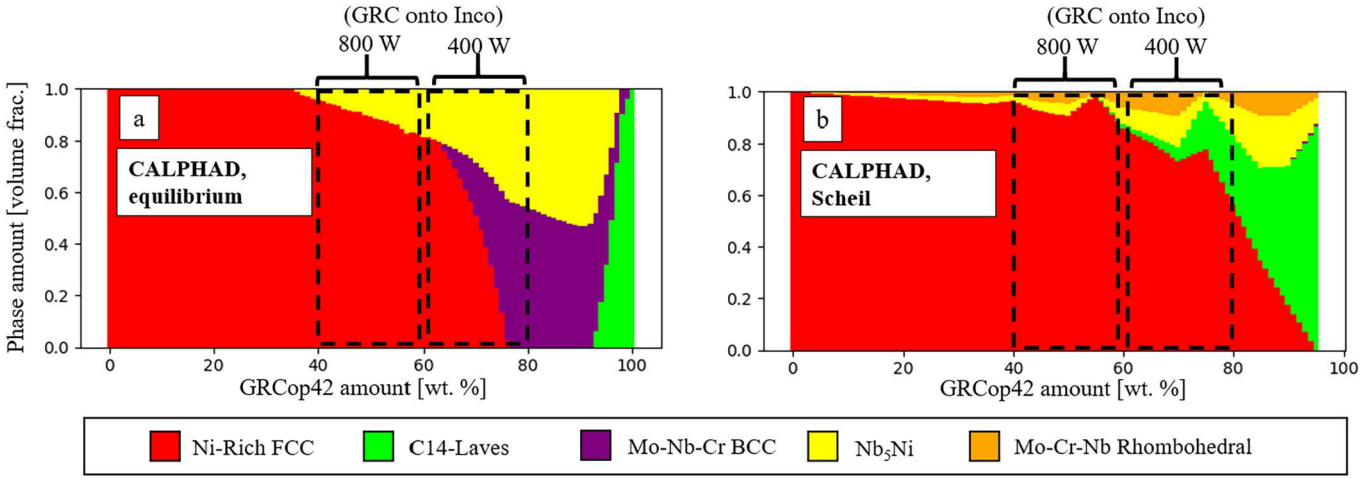

Fig. 11. Phases deriving from Cu-deprived liquid as a function of GRCop42 wt.%, as predicted by CALPHAD for (a) equilibrium at the solidus and (b) Scheil. The dashed line boxes indicate the composition from Fig. 5 above the interface for the GRCop42 onto Inconel 625 joints for 400 W and 800 W.

CRediT authorship contribution statement

Jakub Preis: Writing – original draft, Visualization, Validation, Project administration, Methodology, Investigation, Formal analysis, Conceptualization. **Zexiao Wang:** Investigation. **Jana Howard:** Investigation. **Yu Lu:** Investigation. **Nick Wannenmacher:** Investigation, Writing – review & editing. **Sheng Shen:** Resources. **Brian K. Paul:** Conceptualization, Funding acquisition, Project administration, Resources, Supervision, Writing – review & editing. **Somayeh Pasebani:** Writing – review & editing, Supervision, Conceptualization, Funding acquisition, Investigation, Methodology, Project administration, Resources.

Declaration of competing interest

The authors declare that they have no known competing financial interests or personal relationships that could have appeared to influence the work reported in this paper.

Data availability

Data will be made available on request.

Acknowledgements

This work relates to Department of Navy award (award number N00014-20-1-2836) issued by the Office of Naval Research (ONR). The United States Government has a royalty-free license throughout the world in all copyrightable material contained herein. Any opinions, findings, and conclusions or recommendations expressed in this material are those of the author(s) and do not necessarily reflect the views of the ONR. The authors acknowledge the funding from the National Science Foundation (NSF CAREER award # 2338253). Additionally, this work was supported by Nuclear Science User Facilities at Idaho National Laboratory (award NSUF RTE 22-4400). The authors would like to thank Mr. Jeremy Burgener and Dr. Yaqiao Wo at the Microscopy and Characterization Suite at Boise State University. The corresponding author would like to sincerely acknowledge Mr. Mark Rice and Mrs. Maria Wright for their support and management. The authors thank Peter Eschbach at the OSU electron microscopy center.

Appendix A. Powder micrographs

See Fig. A.1.

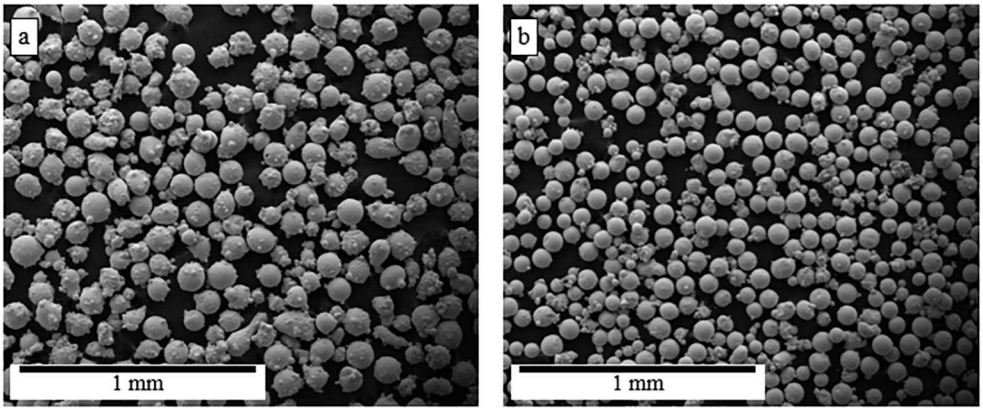

Fig. A.1. SEM micrographs of (a) Inconel 625 powder and (b) GRCop42 powder.

Appendix B. CT scanning of joint

See Fig. B.1.

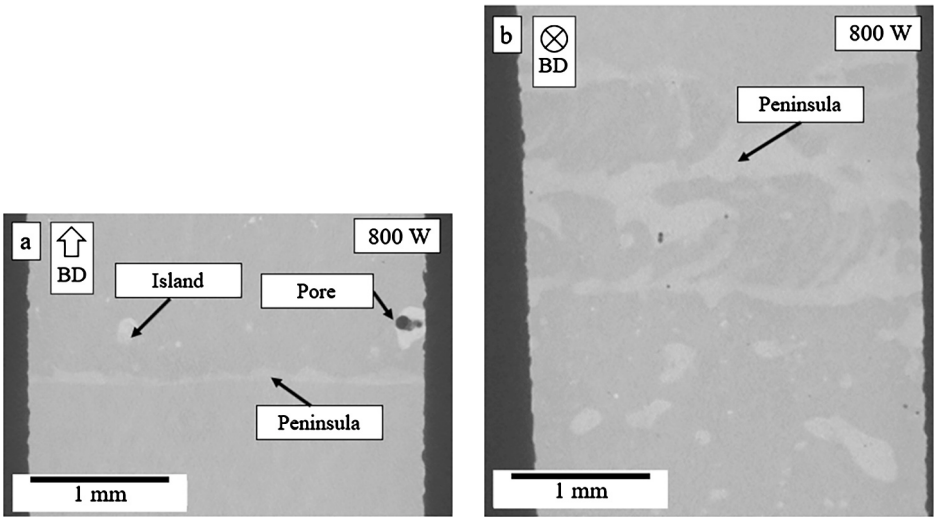

Fig. B.1. CT scan of the 800 W GRCop42 onto Inconel 625 sample showing (a) build direction view and (b) view orthogonal to the build direction (looking downward). The light gray regions correspond to a Cu-deprived composition, while the darker gray region corresponds to Cu-rich composition.

Appendix C. Elemental distribution above the interface

See Fig. C.1.

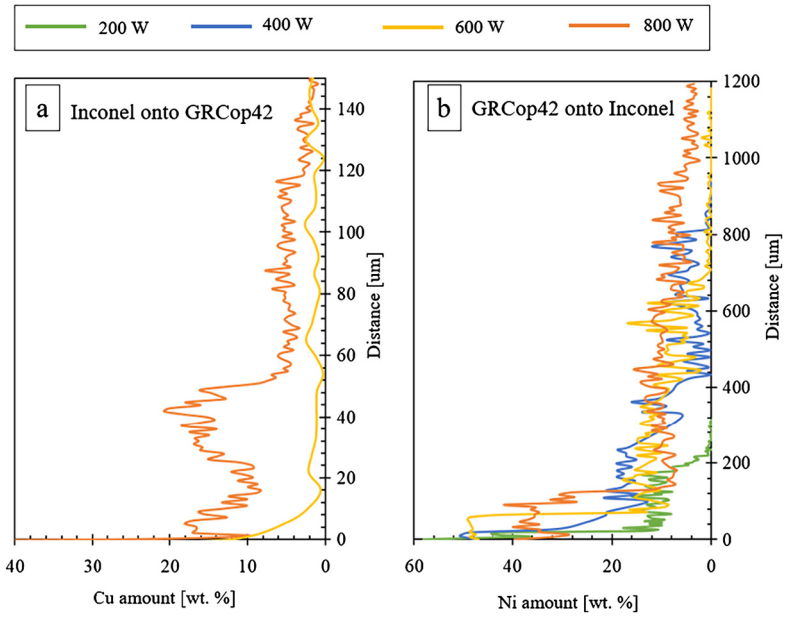

Fig. C.1. EDS line scans above the interface of (a) Cu in Inconel 625 deposited onto GRCop42 and (b) Ni in GRCop42 deposited onto Inconel 625.

References

[1] C. Wei, Z. Zhang, D. Cheng, Z. Sun, M. Zhu, L. Li, An overview of laser-based multiple metallic material additive manufacturing: from macro: from micro-scales, https://doi.org/10.1088/2631-7990/abce04, 2021.

[2] H. Monteiro, G. Carmona-Aparicio, I. Lei, M. Despeisse, Energy and material efficiency strategies enabled by metal additive manufacturing – a review for the aeronautic and aerospace sectors, Energy Rep. 8 (2022), https://doi.org/10.1016/j.egyr.2022.01.035.

[3] P.R. Gradl, C.S. Protz, C.P. Garcia, O.R. Mireles, MartinLeary, introduction to and applications of additive manufacturing for propulsion, in: Metal Additive Manufacturing for Propulsion Applications, Chapter 1, 2022, pp. 1–48, https://arc.aiaa.org/doi/abs/10.2514/5.9781624106279.0001.0048.

[4] P.R. Gradl, C.S. Protz, D.L. Ellis, S.E. Greene, Progress in additively manufactured copper-alloy GRCOP-84, GRCOP-42, and bimetallic combustion chambers for liquid rocket engines, in: Proceedings of the International Astronautical Congress, in: IAC, vol. 2019-October, 2019.

[5] P.R. Gradl, C. Protz, K. Cooper, C. Garcia, D. Ellis, L. Evans, Grcop-42 development and hot-fire testing using additive manufacturing powder bed fusion for channel-cooled combustion chambers, in: AIAA Propulsion and Energy Forum and Exposition, 2019, 2019.

[6] P.R. Gradl, C. Protz, J. Fikes, A. Clark, L. Evans, S. Miller, D. Ellis, T. Hudson, Lightweight thrust chamber assemblies using multi-alloy additive manufacturing and composite overwrap, in: AIAA Propulsion and Energy 2020 Forum, 2020.

[7] P.R. Gradl, T. Teasley, C. Protz, M. Garcia, C. Kantzos, D. Ellis, Advancing GRCop-based bimetallic additive manufacturing to optimize component design and applications for liquid rocket engines, in: AIAA Propulsion and Energy Forum, 2021, 2021.

[8] N. Ghanadi, S. Pasebani, A review on wire-laser directed energy deposition: parameter control, process stability, and future research paths, J. Manuf. Mater. Process. 8 (2) (2024) 84, https://doi.org/10.3390/jmmp8020084.

[9] M. Roccetti Campagnoli, M. Galati, A. Saboori, On the processability of copper components via powder-based additive manufacturing processes: potentials, challenges and feasible solutions, https://doi.org/10.1016/j.jmapro.2021.10.038, 2021.

[10] T. Suresh, S. Landes, T. Letcher, A. Prasad, P. Gradl, D. Ellis, Nanomechanical characterization of additive manufactured grcop-42 alloy developed by directed energy deposition methods, in: ASME International Mechanical Engineering Congress and Exposition, in: Proceedings (IMECE), vol. 4, 2020.

[11] S. Landes, T. Suresh, A. Prasad, T. Letcher, P. Gradl, D. Ellis, Investigation of additive manufactured grcop-42 alloy developed by directed energy deposition methods, in: ASME International Mechanical Engineering Congress and Exposition, in: Proceedings (IMECE), vol. 4, 2020.

[12] D.L. Ellis, G.M. Michal, Mechanical and Thermal Properties of Two Cu-Cr-Nb Alloys and NARloy-Z, NASA Conractor Report 198529, 1996.

[13] G. Demeneghi, B. Barnes, P. Gradl, D. Ellis, J.R. Mayeur, K. Hazeli, Directed energy deposition GRCop-42 copper alloy: characterization and size effects, Mater. Des. 222 (2022), https://doi.org/10.1016/j.matdes.2022.111035.

[14] Y.L. Hu, Y.L. Li, S.Y. Zhang, X. Lin, Z.H. Wang, W.D. Huang, Effect of solution temperature on static recrystallization and ductility of Inconel 625 superalloy fabricated by directed energy deposition, Mater. Sci. Eng. A 772 (2020), https://doi.org/10.1016/j.msea.2019.138711.

[15] A. Theriault, L. Xue, J.R. Dryden, Fatigue behavior of laser consolidated IN-625 at room and elevated temperatures, Mater. Sci. Eng. A 516 (1–2) (2009) 217–225, https://doi.org/10.1016/J.MSEA.2009.03.056.

[16] A. Poudel, P.R. Gradl, S. Shao, N. Shamsaei, Tensile deformation behavior of laser powder direct energy deposited Inconel 625: cryogenic to elevated temperatures, Mater. Sci. Eng. A 889 (2024) 145826, https://doi.org/10.1016/J.MSEA.2023.145826.

[17] K.T. Son, T.Q. Phan, L.E. Levine, K.S. Kim, K.A. Lee, M. Ahlfors, M.E. Kassner, The creep and fracture properties of additively manufactured inconel 625, Materialia 15 (2021) 101021, https://doi.org/10.1016/J.MTLA.2021.101021.

[18] S. Kou, Welding metallurgy, https://doi.org/10.1002/0471434027, 2002.

[19] A. Iams, T. Lienert, D. Otazu, M. Ramoni, Effects of deposition sequence on microstructural evolution in additively manufactured Cu-Cr-Nb alloy / superalloy bimetallic structures, Addit. Manuf. Lett. 6 (2023) 100151, https://doi.org/10.1016/J.ADDLET.2023.100151, https://linkinghub.elsevier.com/retrieve/pii/S2772369023000324.

[20] R. Anderson, J. Terrell, J. Schneider, S. Thompson, P. Gradl, Characteristics of bimetallic interfaces formed during direct energy deposition additive manufacturing processing, Metall. Mater. Trans., B Process Metall. Mater. Proc. Sci. 50 (4) (2019), https://doi.org/10.1007/s11663-019-01612-1.

[21] S. Hales, C. Domack, Electron Beam Freeform Fabrication of Dissimilar Materials: Cracking in Inconel ® 625 Deposited on GRCop-84, 2020.

[22] J. Preis, D. Xu, B.K. Paul, P.A. Eschbach, S. Pasebani, Effect of liquid miscibility gap on defects in Inconel 625–GRCop42 joints through analysis of gradient composition microstructure, J. Manuf. Mater. Process. 8 (1) (2024), https://doi.org/10.3390/jmmp8010042, https://www.mdpi.com/2504-4494/8/1/42.

[23] W. Huang, H. Wang, T. Rinker, W. Tan, Investigation of metal mixing in laser keyhole welding of dissimilar metals, Mater. Des. 195 (2020), https://doi.org/10.1016/j.matdes.2020.109056.

[24] Zexiao Wang, et al., Thermal and microstructural characterization of GRCop-84/In718 Bi-metallic structures additively manufactured by directed energy deposition, JOM 76 (2) (2024) 919–929.

[25] Aaron J. Schmidt, Ramez Cheaito, Matteo Chiesa, A frequency-domain thermoreflectance method for the characterization of thermal properties, Rev. Sci. Instrum. 80 (9) (2009).

[26] Thermo-Calc Software TCCU5 Cu-based Alloys Database.

[27] Thermo-Calc Software TCNI12 Nickel-based Superalloys Database Database.

[28] C. Brink, D.P. Shoemaker, A variation on the σ-phase structure: the crystal structure of the P phase, Mo–Ni–Cr, Acta Crystallogr. 8 (11) (1955), https://doi.org/10.1107/s0365110x55002259.

[29] D. Grüner, A. Ormeci, G. Kreiner, Crystal structure of niobium chromium nickel, Nb(Cr1-xNix)2 (x = 0.49), Z. Kristallogr., New Cryst. Struct. 221 (3) (2014), https://doi.org/10.1524/ncrs.2006.0069.

[30] M.W. Ackerman, T.N. Havill, Thermal conductivity of ten selected binary alloy systems.

[31] I. Gibson, D. Rosen, B. Stucker, M. Khorasani, Additive Manufacturing Technologies, 2021.

[32] B. Cheng, K. Chou, A numerical investigation of thermal property effects on melt pool characteristics in powder-bed electron beam additive manufacturing, Proc. Inst. Mech. Eng., B J. Eng. Manuf. 232 (9) (2018), https://doi.org/10.1177/0954405416673105.

[33] S.H. Ahmed, A. Mian, Influence of material property variation on computationally calculated melt pool temperature during laser melting process, Metals 9 (4) (2019), https://doi.org/10.3390/met9040456.

[34] X. Yan, C. Chang, D. Dong, S. Gao, W. Ma, M. Liu, H. Liao, S. Yin, Microstructure and mechanical properties of pure copper manufactured by selective laser melting, Mater. Sci. Eng. A 789 (2020), https://doi.org/10.1016/j.msea.2020.139615.

[35] A.K. Parida, K. Maity, Comparison the machinability of Inconel 718, Inconel 625 and Monel 400 in hot turning operation, Eng. Sci. Technol., Int. J. 21 (3) (2018) 364–370, https://doi.org/10.1016/J.JESTCH.2018.03.018.

[36] T.W. Nelson, J.C. Lippold, M.J. Mills, Nature and evolution of the fusion boundary in ferritic-austenitic dissimilar weld metals, Part 1 - nucleation and growth, Weld. J. (Miami, Fla) 78 (10) (1999).

[37] A. Kostrivas, J.C. Lippold, Method for studying weld fusion boundary microstructure evolution in aluminum alloys, Weld. J. (Miami, Fla) 79 (1) (2000).

[38] A. Gutierrez, J.C. Lippold, A proposed mechanism for equiaxed grain formation along the fusion boundary in aluminum-copper-lithium alloys, Weld. J. (Miami, Fla) 77 (6) (1998).

[39] N. Chen, H.A. Khan, Z. Wan, J. Lippert, H. Sun, S.L. Shang, Z.K. Liu, J. Li, Microstructural characteristics and crack formation in additively manufactured bimetal material of 316L stainless steel and Inconel 625, Addit. Manuf. 32 (2020), https://doi.org/10.1016/j.addma.2020.101037.

[40] S.K. Rai, A. Kumar, V. Shankar, T. Jayakumar, K.B.S. Rao, B. Raj, Characterization of microstructures in Inconel 625 using X-ray diffraction peak broadening and lattice parameter measurements, Scr. Mater. 51 (1) (2004), https://doi.org/10.1016/j.scriptamat.2004.03.017.

[41] X. Song, S. Feih, W. Zhai, C.N. Sun, F. Li, R. Maiti, J. Wei, Y. Yang, V. Oancea, L. Romano Brandt, A.M. Korsunsky, Advances in additive manufacturing process simulation: residual stresses and distortion predictions in complex metallic components, Mater. Des. 193 (2020) 108779, https://doi.org/10.1016/J.MATDES.2020.108779.